The remediation potential and kinetics of Pb2+ by the organic frameworks of Cladophora rupestris

Lu-sheng Zhang
Anhui Agricultural University
Xiao-yu Feng
Anhui Agricultural University
Chang-fa Qiu
Anhui Agricultural University
Ling-sheng Li
Anhui Agricultural University
Yu Sun
Anhui Agricultural University
Xin-yi Tao
Anhui Agricultural University
Xin-Yue Li
Anhui Agricultural University
Zhao-wen Liu
Chizhou University
deju Cao (cdj@ahau.edu.cn)
Anhui Agricultural University https://orcid.org/0000-0003-0911-0006

Research Article

Keywords: Cladophora rupestris, the organic frameworks, Pb2+, adsorption, functional groups

Posted Date: November 17th, 2023

DOI: https://doi.org/10.21203/rs.3.rs-3424777/v1

Additional Declarations:
Tables 1 to 5 are available in the Supplementary Files section.

Version of Record: A version of this preprint was published at Environmental Science and Pollution Research on January 23rd, 2024. See the published version at https://doi.org/10.1007/s11356-024-32029-2.

The remediation potential and kinetics of Pb^{2+} by the organic frameworks of *Cladophora rupestris*

Lu-sheng Zhang [1], Xiao-yu Feng [1], Chang-fa Qiu [1], Ling-sheng Li [1], Yu Sun [1], Xin-yi Tao [1], Xin-yue Li [1], Zhao-wen Liu [1, 2], De-ju Cao[1*]

[1] Anhui Province Key Laboratory of Farmland Ecological Conservation and Pollution Prevention, School of Resources and Environment, Anhui Agricultural University Hefei 230036, PR China

[2] School of Materials and Environmental Engineering, Chizhou University Chizhou 247000, PR China

Abstract

Cladophora rupestris is ubiquitous in many kinds of waterbodies, and *C. rupestris* biomass can serve as a carrier for adsorbing and transferring heavy metals. In this paper, the organic frameworks of *C. rupestris* (CROF) was produced by treating *C. rupestris* biomass with CH_3COOH. Batch experiments and characterization were performed. Results showed CROF had a specific surface area of 2.58 m^2/g and an external surface area of 2.06 m^2/g. Many mesopores were present in CROF, mainly distributed in 2.5–7.5 nm. The zeta potentials were within the range of −4.46–−13.98 mV in the tested pH of 2.0–9.0. The maximum adsorption capacity (q_{max}) of Pb^{2+} on CROF was 15.02 mg/g, and 97% of Pb^{2+} was adsorbed onto CROF after 25 min. Unexpectedly, CROF could effectively adsorb Pb^{2+} in large pH range. The protein secondary structures and carbon skeletons of CROF all worked in adsorption. The main Pb^{2+} adsorption mechanisms

* Corresponding author. Tel: +86 15922409406; E-mail: cdj@ahau.edu.cn.

were pore filling, electrostatic attraction, Pb–π interaction, and surface complexation. Therefore, it is valuable as a biosorbent for the removal of Pb^{2+} from waterbodies.

Key words: *Cladophora rupestris*, the organic frameworks, Pb^{2+}, adsorption, functional groups

1 Introduction

Heavy metals (HMs) are prevalent inorganic pollutants in water (Fang et al. 2022). Pb^{2+} is one of the substantial HM pollutants that originates from various sources, including gasoline emissions, mining activities, and automobile exhaust (Yang et al. 2022). Due to its non-degradability, high mobility, bioaccumulation, and neurotoxicity (Wang et al. 2022d, Yang et al. 2014), Pb^{2+} has long been a great hazard to public health and the ecology system (Ling et al. 2017). Therefore, the rapid, efficient Pb^{2+} removal is crucial to environmental remediation.

Adsorption is recognized as a highly prospective approach for Pb^{2+} elimination among other HM removal technologies, owing to its operational adaptability, convenient processing, and economic advantages (Yang et al. 2014, Zhang et al. 2022). However, the development of adsorption methods is mainly dependent on the discovery and research of efficient, stable adsorbent materials, such as biochars and various modified biochars (Jiang et al. 2018, Wang et al. 2015, Wu et al. 2021), silicon dioxide (Zeng et al. 2020), metal–organic frameworks (Li et al. 2021b), and even microplastics (Jiang et al. 2022). In addition, polymers are becoming increasingly favored among researchers. Liang et al. (2020) investigated the adsorption behavior of pectin on Pb^{2+} and identified that Pb^{2+} is adsorbed via the ion exchange and surface complexation (Liang et al. 2020). A mesoporous gel bead, incorporating nanocellulose, sodium

alginate, and carboxymethyl–chitosan, was skillfully fabricated to optimize the adsorption efficiency of Cu^{2+} and Pb^{2+} (Li et al. 2021c). However, the above materials and methods either have the disadvantages of chemical reagents that may produce secondary pollution, high cost, or difficult material processing (Demey et al. 2018).

The application of biosorbents for removal of HMs is a great advancement in environmental and bioresource technology (Kim et al. 2015). *Cladophora rupestris* is widely distributed in waterbodies and represents a valuable, renewable biological resource, However, its growth is often uncontrolled and exhibits rapid spread, which can lead to management challenges (Sucaldito &Camacho 2017). *C. rupestris* is an important cellulosic material (Sucaldito &Camacho 2017) with oxygen-containing functional groups (OFGs) and nitrogen-containing functional groups (NFGs) and could efficiently adsorb Pb^{2+} and Cd^{2+} (Cao et al. 2015, Chen et al. 2021a, Zhang et al. 2019a). Biosorbents derived from *C. rupestris* possess a highly porous structure and a higher abundance of exposed functional groups (Sucaldito &Camacho 2017). Therefore, *C. rupestris* biomass holds potential as a promising, sustainable material for the eradication of HMs from waterbodies.

To remove some impurities and not to destroy the macromolecular structure, *C. rupestris* biomass impregnated by CH_3COOH. To the best of our knowledge, the relationship with main adsorption functional groups in higher or lower Pb^{2+} concentrations is not clear.

In this paper, CH_3COOH was used as modifier for *C. rupestris* biomass to produce CROF, and the surface morphology, particle size distribution, and pore structures of

CROF were evaluated by field emission scanning electron microscopy (SEM), laser particle size analyzer (LPSA), and Brunauer–Emmett–Teller (BET), respectively. The adsorption properties of Pb^{2+} were systematically studied by adsorption kinetics, adsorption kinetics, and adsorption thermodynamic. In addition, the relationship between zeta potential and initial pH on adsorption capability was investigated. Finally, the adsorption mechanisms were explored by Fourier transform infrared spectroscopy (FTIR), Emission scanning electron microscopy equipped with energy-dispersive X-ray spectroscopy (SEM–EDS), solid phase ^{13}C nuclear magnetic resonance spectra (NMR), and X-ray photoelectron spectroscopy (XPS) in detail. The results of this paper is benefit for designing green, environmentally friendly biosorbents to adsorb Pb^{2+} from waterbodies.

2 Experimental and methods

2.1 Chemicals

Lead nitrate ($Pb(NO_3)_2$), nitric acid (HNO_3), and sodium hydroxide (NaOH) used in the experiments were analytical purity grade, and obtained from Sinopharm Chemical Reagent Co., ltd. (Shanghai, China). CH_3COOH was bought from Macklin Co., ltd. (Shanghai, China). The 1000 mg/L Pb^{2+} stock solution was synthesized by dissolving 1.599 g of $Pb(NO_3)_2$ in 1000 mL ultrapure water (18.25 MΩ•cm) with 0.01 M sodium nitrate ($NaNO_3$) as the baseline electrolyte. The solutions of various Pb^{2+} concentrations applied in following experiments were obtained by dilution of stock solution.

2.2 Preparation of CROF

C. rupestris was collected from a dam in Hefei city (32°30′ N, 116°17′E, China), washed with running water thoroughly to remove other algae and something dirty, dried at 60 ℃ to constant weight, and crushed into powder. Then, *C. rupestris* biomass and 0.1 M CH_3COOH were fully stirred and mixed in a magnetic stirrer for 2.0 h and washed with ultrapure water until the filtrate was neutral. Next, mixtures filtered and labeled as the organic frameworks of *C. rupestris* (CROF). Finally, CROF were packed in sealed bags as reserves for following use (Fig. S1).

2.3 Adsorption experiments

0.100 g of CROF and 25 ml of Pb^{2+} solution were added to a polypropylene centrifuge tube, and the pH was maintained at 5. Tubes were then placed on oscillator with 180 rpm for 24 h at 25 ℃. Adsorption isotherm experiments were conducted at the initial Pb^{2+} concentrations of 0, 5, 25, 30, 35, 40, 45, and 50 mg/L. Sampling times of 1, 3, 5, 10, 25, 20, 25, 30, 35, 40, 45, 50, 55, and 60 min were used to analyze the adsorption kinetics with 50 mg/L Pb^{2+}. Adsorption thermodynamic experiments were conducted to evaluate the influence of temperature on Pb^{2+} adsorption with the initial Pb^{2+} concentrations of 5, 25, and 50 mg/L at 293, 298, 303, and 308 K. To evaluate the effect of pH on Pb^{2+} adsorption, the mixtures pH was adjusted by 0.1 M HNO_3 and 0.1 M NaOH to 2, 3, 4 5, and 6. In all the experiments, the mixtures were passed through a 0.45 μm aqueous filter, and Pb^{2+} concentrations were measured by a flame atomic adsorption spectrometer (ZEEnit 700P, GER Analytic, Jena) operating at a wavelength of 283.3 nm.

2.4 Characterization methods of CROF

CROF was treated with 0, 5.0, and 50 mg/L Pb^{2+} lyophilized based on freeze dryer (SIM-4, USA).

2.4.1 SEM–EDS characterization

The surface morphology and changes in elemental composition of CROF before and after treatment with 50.0 mg/L Pb^2 adsorption were characterized by SEM (S-4800, Hitachi, Japan) matched EDS (X-MAXN 150, OXFORD, UK) (Yang et al. 2022).

2.4.2 PSD and BET characterization

The evaluation of the particle size distribution for CROF was conducted employing the LPSA (BT–9300H, Bettersize, China), and the analysis of pore structures and specific surface area was undertaken utilizing N_2 adsorption/desorption isotherms in conjunction with BET method (Vario Micro-Cube, Elementar, Germany)(Chen et al. 2021b, Esakkimuthu et al. 2022).

2.4.3 Zeta potential

The zeta potentials of CROF, across a pH spectrum of 2.0 to 9.0 at ambient temperature, was detected based on Zetasizer Nano instrument (Malvern Instruments, Malvern, UK) (Xu et al. 2021).

2.4.4 FTIR spectra and protein secondary structure analysis

0.1 mg CROF treated with 0, 5.0, and 50 mg/L Pb^{2+} were ground in an agate mortar with 0.1 g KBr and then Hydraulically formed into a small disk for FTIR analysis (Nicolette is 50, Thermo Scientific, USA). FTIR data were collected under a resolution of 2 cm^{-1} and a wavenumber of 4000–400 cm^{-1} (Chen et al. 2021a). The protein secondary structures were identified through the analysis of second-derivative spectra

with a wavenumber of 1700–1600 cm^{-1}, typically denoted as the amide I region (Zhang et al. 2019a).

2.4.5 ^{13}C NMR spectroscopy analysis

The ^{13}C NMR were acquired on H/X dual-resonance 4 mm ZrO_2 solid-state probe rotor, rotation speed was 5 kHz, ^{13}C detection resonance frequency was 100.625 MHz, and sampling time was 0.02 s. Spectral width was 50 kHz, cycle delay time was 1 s, and the number of scans was 4096 with 400 MHz (AVANCE III HD, Bruker, Switzerland).

2.4.6 XPS analysis

The surface chemical states of CROF treated with 0, 5.0, and 50 mg/L Pb^{2+} were characterized through XPS (Escalab 250, Thermo-VG Scientific, USA) with the C1s peak calibrated at 284.80 eV (Chen et al. 2021a, Liang et al. 2020).

2.5 Model fitting

2.5.1 Adsorption capacity

The adsorption capacity of Pb^{2+} on CROF was determined via the following formulas (Chen et al. 2021b, Xu et al. 2021):

$$q_t = \frac{(C_0 - C_t)\times \mathrm{V}}{\mathrm{m}}, \quad (1)$$

$$q_e = \frac{(C_0 - C_e)V}{m}, \quad (2)$$

Herein, C_0, C_t, and C_e signify the initial, at the specific time, and at equilibrium time concentrations of Pb^{2+} ($mg{\cdot}L^{-1}$), respectively. V corresponds to the volume of the solution (L), m represents the mass of CROF (g), q_t ($\mathrm{mg}\cdot g^{-1}$) and q_e ($\mathrm{mg}\cdot g^{-1}$)

mean the adsorption capacity of CROF at the specific time and at the equilibrium point, respectively.

2.5.2 Adsorption kinetic models

The adsorption kinetic models were fitted by pseudo-first-order (PFO) model, as shown in Eq. (3); pseudo-second-order (PSO) model, as shown in Eq. (4); and Elovich model, as shown in Eq. (5) (Xu et al. 2021):

$$q_t = q_e(1 - e^{-K_1 t}), \quad (3)$$

$$q_t = K_2 q_e^2 t/(1 + K_2 q_e t), \quad (4)$$

$$q_t = \left(\frac{1}{\beta}\right) In[1 + (\alpha\beta t)], \quad (5)$$

where K_1 (min^{-1}) represents the constant of the PFO model; K_2 ($g \cdot mg^{-1} \cdot min^{-1}$) represents the constant of PSO model, respectively; α ($mg \cdot g^{-1} \cdot min^{-1}$) represents the constant associated with initial adsorption rate of Elovich model; and β ($g \cdot mg^{-1}$) is the constant about coverage and adsorption energy.

1.5.3 Isotherm adsorption models

The Langmuir model, as shown in Eq. (6), the Freundlich model, as shown in Eq. (7), and the Sips model, as shown in Eq. (8), are adopted to simulate the adsorption of Pb^{2+} (Wang et al. 2022c):

$$q_e = \frac{q_{max} K_L C_e}{1 + K_L C_e}, \quad (6)$$

$$q_e = K_f C e^{\frac{1}{n}}, \quad (7)$$

$$q_e = \frac{K_{LF} C_e^n}{1 + \partial_{LF} C_e^n}, \quad (8)$$

$$R_L = \frac{1}{1 + K_L\ C_0}, \quad (9)$$

where q_{max} ($mg \cdot g^{-1}$) denotes the maximum adsorption capacity that originates from Langmuir model; K_L ($L \cdot mg^{-1}$) and K_f ($mg^{1-1/n} \cdot g^{-1} \cdot L^{1/n}$) represent the Langmuir constant and the Freundlich constant, respectively; and n corresponding to the constant associated with the adsorption system. The Langmuir parameter R_L, as shown in Eq. (9), is additionally employed to extend the investigation of the feasibility of the adsorption process (Zhang et al. 2022).

2.5.4 Adsorption thermodynamic models

Thermodynamic parameters such as the Gibbs free energy change (ΔG^{θ}), enthalpy change (ΔH^{θ}), and entropy change (ΔS^{θ}) were computed based on the Van't Hoff formula, as shown in Eqs. (10) and (11), and the Gibbs free energy formula, as shown in Eq. (12) (Abdul Rahim et al. 2020, Zhang et al. 2022):

$$K_T = \frac{q_e}{c_e}, \tag{10}$$

$$In(K_T) = -\left(\frac{\Delta H^{\theta}}{RT}\right) + \left(\frac{\Delta S^{\theta}}{R}\right), \tag{11}$$

$$\Delta G^{\theta} = -\mathrm{RTln}K_T, \tag{12}$$

where K_T refer to the equilibrium constant, and R (8.314 J/mol/K) signifies the ideal gas state constant. The values of ΔH^{θ} and ΔS^{θ} can be determined from the slope and intercept illustrated by the linear relation diagram of $\ln(q_e/c_e)$ versus 1/T.

2.6 Data analysis

The recording and statistical analysis of the experimental data were performed utilizing Microsoft Excel 2010. Peakfit Peak was used to fitting of FTIR and ^{13}C NMR. Avantage was used to process the data of XPS. Origin 2018 was deployed for the simulation of adsorption models and map.

3. Results and discussion

3.1 Characterizations of CROF

The morphology of CROF was characterized by SEM images, and Fig. 1a shows the surface of CROF was rough and had a high porosity and dense fibrous structure, which could increase the adsorption site to HMs (Yang et al. 2022). The particle size distribution of CROF presented a parabolic distribution (Ye et al. 2020) mainly ranging from 23.5 μm to 117.1 μm, with median diameter of 36.8 μm (Fig. 1b).

The porous structure and specific surface area of CROF were investigated by N_2 adsorption/desorption isotherms (Fig. 1c). The curves were type II/IV, and the adsorption began to occur slowly when P/P0 is less than 0.5, which suggested few micropores (<2 nm) in CROF. Hysteresis of type H3 formed within the range of 0.5–1.0, indicating the presence of mesopores in CROF (Jiang et al. 2018), and H3 hysteresis isotherms had no saturation adsorption platform, which suggested that the pore structure had some macropores (Zhou et al. 2022). The specific surface area was 2.58 m^2/g, and the surface area was 2.06, which had a relatively high external surface area (80%), as shown in Table 1. Pore size analysis was performed, as shown in in Fig. 1d, which further proved the presence of micropores and mesoporous structures in CROF. Moreover, mesopore was the dominant pore structure, which mainly distributed in 2.5–7.5 nm on CROF (Li et al. 2021c).

In a word, CROF contains large specific surface area and sophisticated pore structures can be conducive to Pb^{2+} adsorption.

3.2 Adsorption

3.2.1 Adsorption kinetics

The influence of time on Pb^{2+} adsorption is displayed in Fig. 2a. Pb^{2+} adsorption on CROF consisted of three stages. From 0 to 15 min, the adsorption affinity of CROF for Pb^{2+} substantially increased at the first stage. The adsorption amount slightly increased within 15–35 min, and the rate of adsorption progressively slowed at second stage. Then, 97% of the Pb^{2+} was adsorbed onto the CROF within 25 min, and Pb^{2+} adsorption capacity became slower and gravitated toward the adsorption equilibrium after 30 min, which was much faster than that of the other adsorbents (Liang et al. 2020, Wang et al. 2022a, Wang et al. 2022c). The large number of surface adsorption sites available on the CROF may account for the initial rapid adsorption (Spessato et al. 2019, Wang et al. 2022d). As the adsorption site was gradually occupied, the adsorption slowed down and then gradually stabilized.

The PFO, PSO, and Elovich kinetic models were employed to analyze the experimental data and gain further insights into the adsorption. The fitting parameters for each model are presented in Table 2. The correlation coefficient (R^2) of the PFO, PSO, and Elovich kinetic models were 0.75, 0.99, and 0.87, respectively. The fitting results were more consistent with PSO, suggesting chemisorption in the adsorption (Wang et al. 2022b), and chemisorption of Pb^{2+} may regulate the pace of the adsorption (Wang et al. 2022c).

3.2.2 Adsorption isotherms

The effect of initial concentrations of Pb^{2+} on adsorption is presented in Fig. 2b. The value of q_e considerably increased as the concentrations of Pb^{2+} increased and

240 then stabilized, which can be attributed to the large surface area and well-developed
241 pore structure of CROF (Li et al. 2021a). Moreover, the observed trend is consistent
242 with SEM and BET analysis.

243 The Langmuir, Freundlich, and Sips models were used to simulate the effect of
244 initial Pb^{2+} concentrations on adsorption further. The R^2 values of Sips and Langmuir
245 model fitted to Pb^{2+} on CROF (0.96 and 0.94) were better than that of the Freundlich
246 model (0.83), as shown in Table 2, which indicates the Sips model and the Langmuir
247 model could more accurately describe the adsorption (Yang et al. 2021). The Langmuir
248 model assumes adsorption occurs at identical, energetically equivalent sites in a
249 monolayer (Cao et al. 2015). The Sips model is combination of the Langmuir model
250 and the Freundlich model (Demey et al. 2018). A values of 1/n approaching zero is
251 typically indicative of heterogeneous adsorbent, whereas a value closer to 1 is
252 characteristic of adsorbent with relatively homogeneous binding sites. (Demey et al.
253 2018, Karimi et al. 2019). The 1/n value was 1.424, indicating the adsorption of Pb^{2+}
254 by CROF is monolayer surface adsorption. Moreover, the q_{max} of CROF reached
255 15.02 mg/g, consistent with q_e value of 15.01 mg/g The R_L range of CROF was
256 0.012–0.108, indicating this adsorption occurs under beneficial conditions (Zhang et al.
257 2022). The Freundlich constant 1/n was 0.395, indicating the adsorption is favorable
258 (Lin et al. 2022, Yang et al. 2022). Thus, CROF can adsorb Pb^{2+} from waterbodies.

259 **3.2.3 Adsorption thermodynamics**

260 The effect of temperature on Pb^{2+} adsorption and thermodynamic fitting
261 parameters are shown in Fig. 2c and Table 3. ΔG^{θ} (−0.25, −0.23, −0.09, −0.02 kJ/mol)

was negative, indicating the adsorption of Pb^{2+} on CROF is a spontaneous process. ΔG^{θ} values increased from −0.25 kJ mol^{-1} to − 0.02 kJ mol^{-1} as temperature increased from 293K to 308K, indicating low temperature is more conducive to adsorption (Abdul Rahim et al. 2020). ΔH^{θ} (−50.63 kJ·mol^{-1}) was negative, demonstrating the Pb^{2+} adsorption on CROF is an exothermic reaction (Abdul Rahim et al. 2020). ΔS^{θ} (−50.6338kJ·mol^{-1}) was negative, illustrating the degree of freedom at the solid–liquid interface is reduced during the Pb^{2+} adsorption (Chen et al. 2021b).

3.2.4 Effect of initial pH on adsorption capability

The zeta potential plots can determine the influence of pH over CROF surface charge and evaluate the degree of carboxyl group deprotonation and amine protonation (Liang et al. 2020). Fig. 3a shows the zeta potentials of CROF decreased remarkably with increasing pH (2–9) and were markedly negative within the range of −4.46–−13.98 mV. Thus, CROF can generate electrostatic attraction with Pb^{2+} (Yang et al. 2014) in the tested pH range.

The pH is also an important parameter about adsorption because pH affects not only the binding status of functional groups of CROF with H^{+}, but also the speciation of Pb^{2+} in the solutions (Liang et al. 2020). The concentrations of Pb^{2+} were set below 6 to exclude the effect of Pb^{2+} precipitation in the experiments. The effect of initial pH on Pb^{2+} adsorption capability is presented in Fig. 3b. The quantity of Pb^{2+} adsorbed by CROF increased from 9.36 mg/g to 13.01 mg/g and then stabilized by increasing the solution pH. CROF maintained a relatively stable adsorption capability of Pb^{2+} in a wide pH range.

The degree of carboxyl deprotonation and amino protonation increased, and electrostatic interaction consequently increased, showing the increase of Pb^{2+} adsorption capability as the pH increased (Wu et al. 2021, Xu et al. 2021).

3.3 Adsorption mechanisms

3.3.1 Morphology and analysis of major elements

Fig. 4. shows the SEM-EDS analysis of CROF before and after adsorption of 50 mg/L Pb^{2+}. The surface of CROF became darker, compact, and smooth, and the pore was gradually filled after adsorption of Pb^{2+}. The EDS analysis of CROF verified Pb^{2+} was successfully adsorbed on CROF surface with carbon (C) and oxygen (O) as the main elements. The contents of C and O of CROF treated with 50 mg/L Pb^{2+} decreased from 81.6 wt% and 18.4 wt% to 79.3 wt% and 17.1 wt% compared with CROF treated with 0 mg/L Pb^{2+}, and 3.7 wt% Pb^{2+} was detected on the CROF surface. The adsorbed Pb^{2+} decreased along with the lower C and O content on the CROF surface, indicating CROF can adsorb Pb^{2+} effectively, and the adsorption ability might relate to the C and O content on CROF surface (Wang et al. 2023).

3.3.2 FTIR and protein secondary structure analysis

Fig. 5. shows the FTIR spectra of CROF treated with 0, 5.0, and 50 mg/L Pb^{2+}. The peak at 3350.06 cm^{-1}, which is attributed to the vibrations of -NH_2 and -OH groups (Wang et al. 2022c), shifted to 3405.94 and 3348.83 cm^{-1} and weakened after CROF was treated with 5.0 and 50.0 mg/L Pb^{2+}, respectively. This result indicates the binding affinity of Pb^{2+} toward -OH and –NH groups (Liang et al. 2020). The peak observed at 2923 cm^{-1} corresponds to the stretching vibration of -CH and -CH2 groups presented

306 in lignin and polysaccharides (Zong et al. 2020), and these heterocyclic compounds
307 could promptly bond with Pb^{2+} because they possess a weak cation binder (Yang et al.
308 2021). The adsorption of C=C groups is often associated with the peak at 1647.85 cm^{-1},
309 and the peak at 1637.31 cm^{-1} is typically attributed to carbonyl/carboxyl C=O groups
310 (Wang et al. 2021). The characteristic peak of CROF, which was originally observed
311 at 1640.28 cm^{-1}, shifted to 1637.31 cm^{-1} after CROF was treated with 5 mg/L Pb^{2+}.
312 This shift demonstrates the occurrence of electrostatic attraction or complexation
313 between the lone pairs of electrons on the carbonyl group (C=O) and the unoccupied
314 orbitals of Pb^{2+} (Tang et al. 2022). Unexpectedly, the peak oppositely shifted to 1647
315 cm^{-1} after CROF was treated with 50 mg/L Pb^{2+}. This remarkable shift may be
316 attributed to the formation of Pb–π interactions (Wang et al. 2021) between aromatic
317 rings or conjugated systems of CROF and Pb^{2+}.

318 The stretching vibration of C-O peak at 1249.50 cm^{-1} (Qin et al. 2020, Yang et
319 al. 2020) exhibited a blueshift, suggesting the C-O groups of esters and aromatic
320 hydrocarbons could form complexes with Pb^{2+}.

321 More detailed information on the protein secondary structures obtained through
322 Gaussian fitting and the fitted curves are presented in Figs. 5b–d. The peaks at 1630.11,
323 1651.11, and 1672.56 cm^{-1} are attributed to β-sheet, α-helix, and β-turn in protein
324 secondary structures (Zhang et al. 2019b), respectively, and the relative concentrations
325 are listed in Table 2.

326 The fitted curves of CROF treated with 0, 5.0, and 50 mg/L Pb^{2+} had similar
327 protein secondary structures (Fig. 5b–d) and proportions (Table 4) due to a batch of

materials. CROF treated with 0 mg/L Pb^{2+} had less percentage of β-sheet and β-turn (29.3% and 23.8%, respectively) and more α-helix (44.0%). A lower value of α-helix/(β-sheet + random coil) value is commonly considered an indicator for looser protein (Wang et al. 2020). The protein secondary structure is mainly maintained by hydrogen bonding interactions (Chen et al. 2021a). Through computational analysis, CROF treated with 0 mg/L Pb^{2+} exhibited the most compact structure, as evidenced by the highest α-helix/(β-sheet + random coil) value of 1.52. By contrast, CROF treated with 5.0, and 50 mg/L Pb^{2+} displayed a looser structure with similar α-helix/(β-sheet + random coil) values of 1.22 and 1.21, respectively. Pb^{2+} disrupted the hydrogen bonding of CROF, making the protein secondary structures looser, and the loose protein exposed more intrinsic functional groups to bind to Pb^{2+} (Hou et al. 2015, Xiao et al. 2019).

3.3.2 Polysaccharide analysis

Fig. 6 shows the ^{13}C NMR spectra of CROF treated with 0, 5.0, and 50 mg/L Pb^{2+}. The ^{13}C NMR peaks of CROF are mainly distributed in the alkyl-C (30.5 ppm), O-alkyl-C (54.9 ppm), HCOH-C (65.3 and 72.7 ppm), and anomeric-C (105.5 ppm) regions (Wang et al. 2023). With the increase of Pb^{2+} concentrations, the relative intensities of HCOH-C and carbonyl-C signal peaks weakened, which may be due to formed the Pb–OOC complex (Chen et al. 2021a). In Table 5, the proportion of aromatic-C decreased from 4.24% to 3.54% after CROF was treated with 5.0 mg/L Pb^{2+} and increased to 4.72% after CROF was treated with 50 mg/L Pb^{2+}, indicating the presence of Pb–π interaction, which agrees with FTIR analysis. In addition, with the increase of Pb^{2+} concentrations, the proportion of alkyl-C of CROF increased from 10

52% to 12 77% and 13.18%, and the proportion of O-alkyl-C increased from 6 43% to 7.21% and 7.51%. Therefore, OFGs in the carbohydrates of CROF could complex with Pb^{2+}, and as a result, showed exposure of more alkyl (Prietzel et al. 2018).

3.3.4 Functional group analysis

The XPS spectra were used for further revealing the adsorption mechanisms of Pb^{2+} on CROF. Fig. 7a shows Pb4f was observed under 5.0 mg/L and 50.0 mg/L Pb^{2+}, indicating the successful adsorption of Pb^{2+} on CROF. These findings agree with SEM-EDX analysis. The binding energy between 136 and 144 eV has the possible states of Pb^{2+}, O-Pb, and N-Pb (Fig. 7b) (Jiang et al. 2019, Liang et al. 2020).

In the spectra of C1s (Fig. 8a), four C peaks of C=C/C-H (~284.80 eV), C-O/C-N (~286.33 eV), C=O/N-C=O/O-C-O (~287.9 eV), and O-C=O (~289.49 eV) varied at different Pb^{2+} concentrations (Cai et al. 2021, Ling et al. 2017, Song et al. 2021, Tang et al. 2022). With the increase of Pb^{2+} concentrations, the proportion of C-O/C-N decreased from 30.14% to 26.40% and 27.64% (Fig. 8b). Conversely, the proportion of C=C/C-H and O-C=O increased. Hence, Pb–π interaction existed between CROF and Pb^{2+} (Wang et al. 2015), which matched the ^{13}C NMR analyses.

The O1s spectrum displayed distinct peaks that can be assigned to two specific functional groups. One peak appeared at approximately 531.4 eV and corresponds to the N-C=O functional groups. Additionally, the other peak was around 532 eV, which can be attributed to the C-O-C/C-O-H functional groups (Fig. 8c) (Liang et al. 2020, Song et al. 2021). The binding energy increased after CROF was treated with 5.0 mg/L and 50 mg/L Pb^{2+}, which indicated complexation between Pb^{2+} and OFGs (Tang et al.

372 2021). At the time, the proportion of C-O-C/C-O-H decreased from 49.14% to 43.34%
373 after CROF was treated with 5.0 mg/L Pb^{2+}. Similarly, the proportion of N-C=O
374 decreased from 50.86% to 47.88% after CROF was treated with 50 mg/L Pb^{2+} (Fig. 8d).
375 Therefore, C-O-C/C-O-H groups primarily bind with Pb^{2+} at lower Pb^{2+} concentrations,
376 whereas N-C=O groups play a major role at higher Pb^{2+} concentrations.

377 In the spectra of N1s (Fig. 8e), the peak corresponding to N-C=O with a binding
378 energy of 399.86 eV and the peak corresponding to -NH_2 with a binding energy of
379 400.58 eV increased with the increase of Pb^{2+} concentrations (Li et al. 2021c, Song et
380 al. 2021). This phenomenon can be attributed to interaction between Pb^{2+} and the N
381 atom, where Pb^{2+} empty orbital received one pair of electrons from the N atom.
382 Therefore, the electron density of N atom decreased, and the binding energy increased
383 (Zhou et al. 2005). The proportion of NH_3^- decreased and disappeared after CROF was
384 treated with 5.0 and 50.0 mg/L Pb^{2+} (Fig. 8f), respectively, which may be due to its
385 transformation into metal complexes (Gao et al. 2017, Wang et al. 2022a).

386 **3.3.4 Simulation of Pb^{2+} adsorbed by CROF**

387 The results of the above gradual exploration reveal polysaccharide and protein of
388 CROF play an important role in the adsorption of Pb^{2+}. Different major functional
389 groups act in relatively high and relatively low Pb^{2+} concentration solutions.
390 Specifically, surface complexation with C-O-C/ C-O-H, -NH_2, and NH_3^- was
391 relatively dominant after CROF was treated with lower Pb^{2+} concentrations (≤5 mg/L);
392 Pb–π interaction and surface complexation with N-C=O strengthened after CROF was

393 treated with higher Pb^{2+} concentrations (50 mg/L). Pore filling and electrostatic
394 attraction work at higher and lower Pb^{2+}concentrations (Fig. 9).

395 **4 Conclusions**

396 CROF was formed by treating *C. rupestris* biomass with CH_3COOH. The
397 adsorption equilibrium time of Pb^{2+} was 25 min, which was faster than that of other
398 adsorbents. The q_{max} of Pb^{2+} was 15.02 mg/g, and CROF had more mesoporous
399 structure and relatively high external surface area. CROF also could adsorb Pb^{2+} in a
400 wide pH range with low markedly negative zeta potentials, which promoted the
401 effective adsorption of Pb^{2+}. The main Pb^{2+} adsorption mechanisms were pore filling,
402 electrostatic attraction, Pb–π interaction, and surface complexation with proteins and
403 polysaccharides. Specifically, surface complexation with C-O-C/C-O-H, $-NH_2$, and
404 NH_3^- was relatively dominant after CROF was treated with lower Pb^{2+} concentrations
405 (≤5 mg/L); Pb–π interaction strengthened and surface complexed with N-C=O after
406 CROF was treated with higher Pb^{2+} concentrations (50 mg/L). This paper provided a
407 new ideal of natural polymers biosorbents for Pb^{2+}. Therefore, CROF is a promising
408 biosorbent to adsorb Pb^{2+} from waterbodies.

409 **References**

410 Abdul Rahim AR, Mohsin HM, Thanabalan M, Rabat NE, Saman N, Mat H, Johari K (2020):
411 Effective carbonaceous desiccated coconut waste adsorbent for application of heavy metal
412 uptakes by adsorption: Equilibrium, kinetic and thermodynamics analysis. Biomass and
413 Bioenergy 142, 105805.http://doiorg/10.1016/j.biombioe.2020.105805.
414 Cai T, Liu X, Zhang J, Tie B, Lei M, Wei X, Peng O, Du H (2021): Silicate-modified oiltea camellia
415 shell-derived biochar: A novel and cost-effective sorbent for cadmium removal. Journal of
416 Cleaner Production 281, 125390.http://doiorg/10.1016/j.jclepro.2020.125390.
417 Cao DJ, Shi XD, Li H, Xie PP, Zhang HM, Deng JW, Liang YG (2015): Effects of lead on tolerance,
418 bioaccumulation, and antioxidative defense system of green algae, Cladophora. Ecotoxicol
419 Environ Saf 112, 231-7.http://doiorg/10.1016/j.ecoenv.2014.11.007.

Chen QY, Yang L, Liu L, Qian LW, Tian KL, Zhang Q, Cao DJ (2021a): Combined forms of Pb and its detoxification and absorption in Cladophora rupestris subcells. Spectrochim Acta A Mol Biomol Spectrosc 248, 119190.http://doiorg/10.1016/j.saa.2020.119190.

Chen Y, Tang J, Wang S, Zhang L, Sun W (2021b): Bimetallic coordination polymer for highly selective removal of Pb(II): Activation energy, isosteric heat of adsorption and adsorption mechanism. Chemical Engineering Journal 425, 131474.http://doiorg/10.1016/j.cej.2021.131474.

Demey H, Vincent T, Guibal E (2018): A novel algal-based sorbent for heavy metal removal. Chemical Engineering Journal 332, 582-595.http://doiorg/10.1016/j.cej.2017.09.083.

Esakkimuthu ES, DeVallance D, Pylypchuk I, Moreno A, Sipponen MH (2022): Multifunctional lignin-poly (lactic acid) biocomposites for packaging applications. Front Bioeng Biotechnol 10, 1025076.http://doiorg/10.3389/fbioe.2022.1025076.

Fang Y, Ren G, Ma Y, Wang C, Li M, Pang X, Pan Q, Li J (2022): Adsorption and reutilization of Pb(II) based on acid-resistant metal-organic gel. Separation and Purification Technology 295, 121253.http://doiorg/10.1016/j.seppur.2022.121253.

Gao X, Zhang Y, Zhao Y (2017): Biosorption and reduction of Au (III) to gold nanoparticles by thiourea modified alginate. Carbohydr Polym 159, 108-115.http://doiorg/10.1016/j.carbpol.2016.11.095.

Hou X, Liu S, Zhang Z (2015): Role of extracellular polymeric substance in determining the high aggregation ability of anammox sludge. Water Res 75, 51-62.http://doiorg/10.1016/j.watres.2015.02.031.

Jiang B, Lin Y, Mbog JC (2018): Biochar derived from swine manure digestate and applied on the removals of heavy metals and antibiotics. Bioresour Technol 270, 603-611.http://doiorg/10.1016/j.biortech.2018.08.022.

Jiang B, Gong Y, Gao J, Sun T, Liu Y, Oturan N, Oturan MA (2019): The reduction of Cr(VI) to Cr(III) mediated by environmentally relevant carboxylic acids: State-of-the-art and perspectives. J Hazard Mater 365, 205-226.http://doiorg/10.1016/j.jhazmat.2018.10.070.

Jiang Y, Qin Z, Fei J, Ding D, Sun H, Wang J, Yin X (2022): Surfactant-induced adsorption of Pb(II) on the cracked structure of microplastics. J Colloid Interface Sci 621, 91-100.http://doiorg/10.1016/j.jcis.2022.04.068.

Karimi S, Tavakkoli Yaraki M, Karri RR (2019): A comprehensive review of the adsorption mechanisms and factors influencing the adsorption process from the perspective of bioethanol dehydration. Renewable and Sustainable Energy Reviews 107, 535-553.http://doiorg/10.1016/j.rser.2019.03.025.

Kim N, Park M, Park D (2015): A new efficient forest biowaste as biosorbent for removal of cationic heavy metals. Bioresour Technol 175, 629-32.http://doiorg/10.1016/j.biortech.2014.10.092.

Li B, Zhang Y, Xu J, Mei Y, Fan S, Xu H (2021a): Effect of carbonization methods on the properties of tea waste biochars and their application in tetracycline removal from aqueous solutions. Chemosphere 267, 129283.http://doiorg/10.1016/j.chemosphere.2020.129283.

Li J, Zhang Y, Zhou Y, Fang F, Li X (2021b): Tailored metal-organic frameworks facilitate the simultaneously high-efficient sorption of UO(2)(2+) and ReO(4)(-) in water. Sci Total Environ 799, 149468.http://doiorg/10.1016/j.scitotenv.2021.149468.

Li W, Zhang L, Hu D, Yang R, Zhang J, Guan Y, Lv F, Gao H (2021c): A mesoporous nanocellulose/sodium alginate/carboxymethyl-chitosan gel beads for efficient adsorption

of Cu(2+) and Pb(2). Int J Biol Macromol 187, 922-930.http://doiorg/10.1016/j.ijbiomac.2021.07.181.

Liang RH, Li Y, Huang L, Wang XD, Hu XX, Liu CM, Chen MS, Chen J (2020): Pb(2+) adsorption by ethylenediamine-modified pectins and their adsorption mechanisms. Carbohydr Polym 234, 115911.http://doiorg/10.1016/j.carbpol.2020.115911.

Lin X, Shen T, Li M, Shaoyu J, Zhuang W, Li M, Xu H, Zhu C, Ying H, Ouyang P (2022): Synthesis, characterization, and utilization of poly-amino acid-functionalized lignin for efficient and selective removal of lead ion from aqueous solution. Journal of Cleaner Production 347, 131219.http://doiorg/10.1016/j.jclepro.2022.131219.

Ling LL, Liu WJ, Zhang S, Jiang H (2017): Magnesium Oxide Embedded Nitrogen Self-Doped Biochar Composites: Fast and High-Efficiency Adsorption of Heavy Metals in an Aqueous Solution. Environ Sci Technol 51, 10081-10089.http://doiorg/10.1021/acs.est.7b02382.

Prietzel J, Muller S, Kogel-Knabner I, Thieme J, Jaye C, Fischer D (2018): Comparison of soil organic carbon speciation using C NEXAFS and CPMAS (13)C NMR spectroscopy. Sci Total Environ 628-629, 906-918.http://doiorg/10.1016/j.scitotenv.2018.02.121.

Qin J, Li Q, Liu Y, Niu A, Lin C (2020): Biochar-driven reduction of As(V) and Cr(VI): Effects of pyrolysis temperature and low-molecular-weight organic acids. Ecotoxicol Environ Saf 201, 110873.http://doiorg/10.1016/j.ecoenv.2020.110873.

Song J, Messele SA, Meng L, Huang Z, Gamal El-Din M (2021): Adsorption of metals from oil sands process water (OSPW) under natural pH by sludge-based Biochar/Chitosan composite. Water Res 194, 116930.http://doiorg/10.1016/j.watres.2021.116930.

Spessato L, Bedin KC, Cazetta AL, Souza I, Duarte VA, Crespo LHS, Silva MC, Pontes RM, Almeida VC (2019): KOH-super activated carbon from biomass waste: Insights into the paracetamol adsorption mechanism and thermal regeneration cycles. J Hazard Mater 371, 499-505.http://doiorg/10.1016/j.jhazmat.2019.02.102.

Sucaldito MR, Camacho DH (2017): Characteristics of unique HBr-hydrolyzed cellulose nanocrystals from freshwater green algae (Cladophora rupestris) and its reinforcement in starch-based film. Carbohydr Polym 169, 315-323.http://doiorg/10.1016/j.carbpol.2017.04.031.

Tang S, Lin L, Wang X, Yu A, Sun X (2021): Interfacial interactions between collected nylon microplastics and three divalent metal ions (Cu(II), Ni(II), Zn(II)) in aqueous solutions. J Hazard Mater 403, 123548.http://doiorg/10.1016/j.jhazmat.2020.123548.

Tang S, Yang X, Zhang T, Qin Y, Cao C, Shi H, Zhao Y (2022): Adsorption mechanisms of metal ions (Pb, Cd, Cu) onto polyamide 6 microplastics: New insight into environmental risks in comparison with natural media in different water matrices. Gondwana Research 110, 214-225.http://doiorg/10.1016/j.gr.2022.06.017.

Wang Q, Wang Y, Yang Z, Han W, Yuan L, Zhang L, Huang XJCEJA (2022a): Efficient removal of Pb (II) and Cd (II) from aqueous solutions by mango seed biosorbent. Chemical Engineering Journal Advances 11, 100295. https://doi.org/10.1016/j.ceja.2022.100295

Wang Q, Zhang Y, Chen H, Chen S, Wang Y (2023): Effects of humic acids on the adsorption of Pb(II) ions onto biofilm-developed microplastics in aqueous ecosystems. Sci Total Environ 882, 163466.http://doiorg/10.1016/j.scitotenv.2023.163466.

Wang S, Wang H, Wang S, Zhang L, Fu L (2022b): Highly effective and selective adsorption of Au(III) from aqueous solution by poly(ethylene sulfide) functionalized chitosan: Kinetics,

isothermal adsorption and thermodynamics. Microporous and Mesoporous Materials 341, 112074.http://doiorg/10.1016/j.micromeso.2022.112074.

Wang W, Yan Y, Zhao Y, Shi Q, Wang Y (2020): Characterization of stratified EPS and their role in the initial adhesion of anammox consortia. Water Res 169, 115223.http://doiorg/10.1016/j.watres.2019.115223.

Wang X, Zhang H, He Q, Xing H, Feng K, Guo F, Wang W (2022c): Core-shell alginate beads as green reactor to synthesize grafted composite beads to efficiently boost single/co-adsorption of dyes and Pb(II). Int J Biol Macromol 206, 10-20.http://doiorg/10.1016/j.ijbiomac.2022.02.091.

Wang Y, van Zwieten L, Wang H, Wang L, Li R, Qu J, Zhang Y (2022d): Sorption of Pb(II) onto biochar is enhanced through co-sorption of dissolved organic matter. Sci Total Environ 825, 153686.http://doiorg/10.1016/j.scitotenv.2022.153686.

Wang Z, Liu G, Zheng H, Li F, Ngo HH, Guo W, Liu C, Chen L, Xing B (2015): Investigating the mechanisms of biochar's removal of lead from solution. Bioresour Technol 177, 308-17.http://doiorg/10.1016/j.biortech.2014.11.077.

Wang Z, Xu J, Yellezuome D, Liu R (2021): Effects of cotton straw-derived biochar under different pyrolysis conditions on Pb (II) adsorption properties in aqueous solutions. Journal of Analytical and Applied Pyrolysis 157, 105214.http://doiorg/10.1016/j.jaap.2021.105214.

Wu F, Chen L, Hu P, Wang Y, Deng J, Mi B (2021): Industrial alkali lignin-derived biochar as highly efficient and low-cost adsorption material for Pb(II) from aquatic environment. Bioresour Technol 322, 124539.http://doiorg/10.1016/j.biortech.2020.124539.

Xiao B, Liu Y, Luo M, Yang T, Guo X, Yi H (2019): Evaluation of the secondary structures of protein in the extracellular polymeric substances extracted from activated sludge by different methods. J Environ Sci (China) 80, 128-136.http://doiorg/10.1016/j.jes.2018.12.003.

Xu X, Ouyang X-k, Yang L-YJJoML (2021): Adsorption of Pb (II) from aqueous solutions using crosslinked carboxylated chitosan/carboxylated nanocellulose hydrogel beads. Journal of Molecular Liquids 322, 114523. http://doiorg/10.1016/j.molliq.2020.114523.

Yang G, Zhang N, Yang J, Fu Q, Wang Y, Wang D, Tang L, Xia J, Liu X, Li X, Yang Q, Liu Y, Wang Q, Ni BJ (2020): Interaction between perfluorooctanoic acid and aerobic granular sludge. Water Res 169, 115249.http://doiorg/10.1016/j.watres.2019.115249.

Yang X, Chen L, Ren D, Wang S, Ren Z (2022): Adsorption of Pb(II) from water by treatment with an O-hydroxyphenyl thiourea-modified chitosan. Int J Biol Macromol 220, 280-290.http://doiorg/10.1016/j.ijbiomac.2022.08.090.

Yang Y, Wei Z, Zhang X, Chen X, Yue D, Yin Q, Xiao L, Yang L (2014): Biochar from Alternanthera philoxeroides could remove Pb(II) efficiently. Bioresour Technol 171, 227-32.http://doiorg/10.1016/j.biortech.2014.08.015.

Yang Z, Hou J, Wu J, Miao L (2021): The effect of carbonization temperature on the capacity and mechanisms of Pb(II) adsorption by microalgae residue-derived biochar. Ecotoxicol Environ Saf 225, 112750.http://doiorg/10.1016/j.ecoenv.2021.112750.

Ye Z, Liu L, Tan Z, Zhang L, Huang Q (2020): Effects of pyrolysis conditions on migration and distribution of biochar nitrogen in the soil-plant-atmosphere system. Sci Total Environ 723, 138006.http://doiorg/10.1016/j.scitotenv.2020.138006.

Zeng Q, Huang Y, Huang L, Li S, Hu L, Xiong D, Zhong H, He Z (2020): A novel composite of

SiO(2) decorated with nano ferrous oxalate (SDNF) for efficient and highly selective removal of Pb(2+) from aqueous solutions. J Hazard Mater 391, 122193.http://doiorg/10.1016/j.jhazmat.2020.122193.

Zhang HM, Geng G, Wang JJ, Xin Y, Zhang Q, Cao DJ, Ma YH (2019a): The remediation potential and kinetics of cadmium in the green alga Cladophora rupestris. Environ Sci Pollut Res Int 26, 775-783.http://doiorg/10.1007/s11356-018-3661-z.

Zhang J, Li M, Li C, Liu Y (2019b): Effect of wheat bran insoluble dietary fiber with different particle size on the texture properties, protein secondary structure, and microstructure of noodles. Grain & Oil Science and Technology 2, 97-102.http://doiorg/10.1016/j.gaost.2019.10.001.

Zhang S, Arkin K, Zheng Y, Ma J, Bei Y, Liu D, Shang Q (2022): Preparation of a composite material based on self-assembly of biomass carbon dots and sodium alginate hydrogel and its green, efficient and visual adsorption performance for Pb2+. Journal of Environmental Chemical Engineering 10, 106921.http://doiorg/10.1016/j.jece.2021.106921.

Zhou D, Zhang L, Guo S (2005): Mechanisms of lead biosorption on cellulose/chitin beads. Water Res 39, 3755-62.http://doiorg/10.1016/j.watres.2005.06.033.

Zhou Y, Fang F, Lv Q, Zhang Y, Li X, Li J (2022): Simultaneous removal of tetracycline and norfloxacin from water by iron-trimesic metal-organic frameworks. Journal of Environmental Chemical Engineering 10, 107403.http://doiorg/10.1016/j.jece.2022.107403.

Zong P, Jiang Y, Tian Y, Li J, Yuan M, Ji Y, Chen M, Li D, Qiao Y (2020): Pyrolysis behavior and product distributions of biomass six group components: Starch, cellulose, hemicellulose, lignin, protein and oil. Energy Conversion and Management 216, 112777.http://doiorg/10.1016/j.enconman.2020.112777.

Ethical Approval

Not applicable.

Consent to Participate

We consent to participate this manuscript.

Consent to Publish

We consent to publish this manuscript.

Authors Contributions

Lu-sheng Zhang: Methodology, Writing - original draft, Investigation. Xiao-yu Feng: Software, Formal analysis. Ling-sheng Li: Formal analysis, Software. Yu Sun: Formal analysis, Visualization. Xin-yi Tao: Formal analysis, Visualization. Xin-yue Li:

Revising, Conceptualization. Zhao-wen Liu: Resources, Writing - review & editing, Supervision, Data curation. De-ju Cao: Resources, Writing - review & editing, Supervision, Data curation.

Funding

This work was under Natural Science Foundation of China (41877418), the financial aid of Nature Fund of Anhui Province of China (1808085MD100),Materials and Chemical Engineering First-class Undergraduate Talent Demonstration and Leading Base(2020rcsfjd28), School-level key projects of Chizhou College (CZ2023ZRZ01,CZ2021ZRZ12) and Funding for this study was provided by Natural Students' Innovation and Entrepreneurship Training Program (X202210364125；X202210364133) also.

Competing Interests

The authors declare that they have no conflict of interest.

Availability of data and materials

We declared that the data and materials presented in this paper are reliable.

Figures

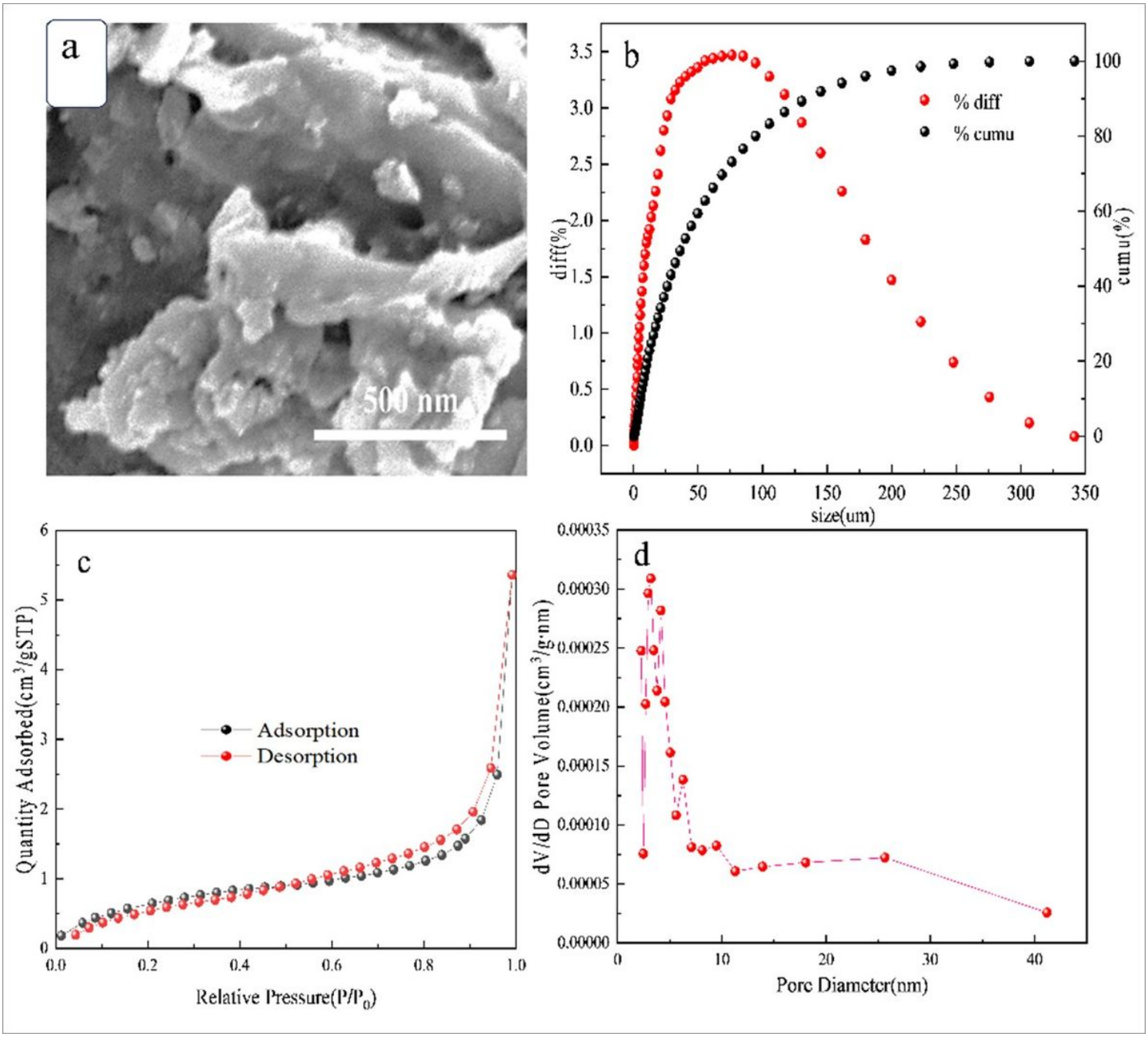

Figure 1

SEM images (a), particle size distribution (b) and BET (c, d) of CROF.

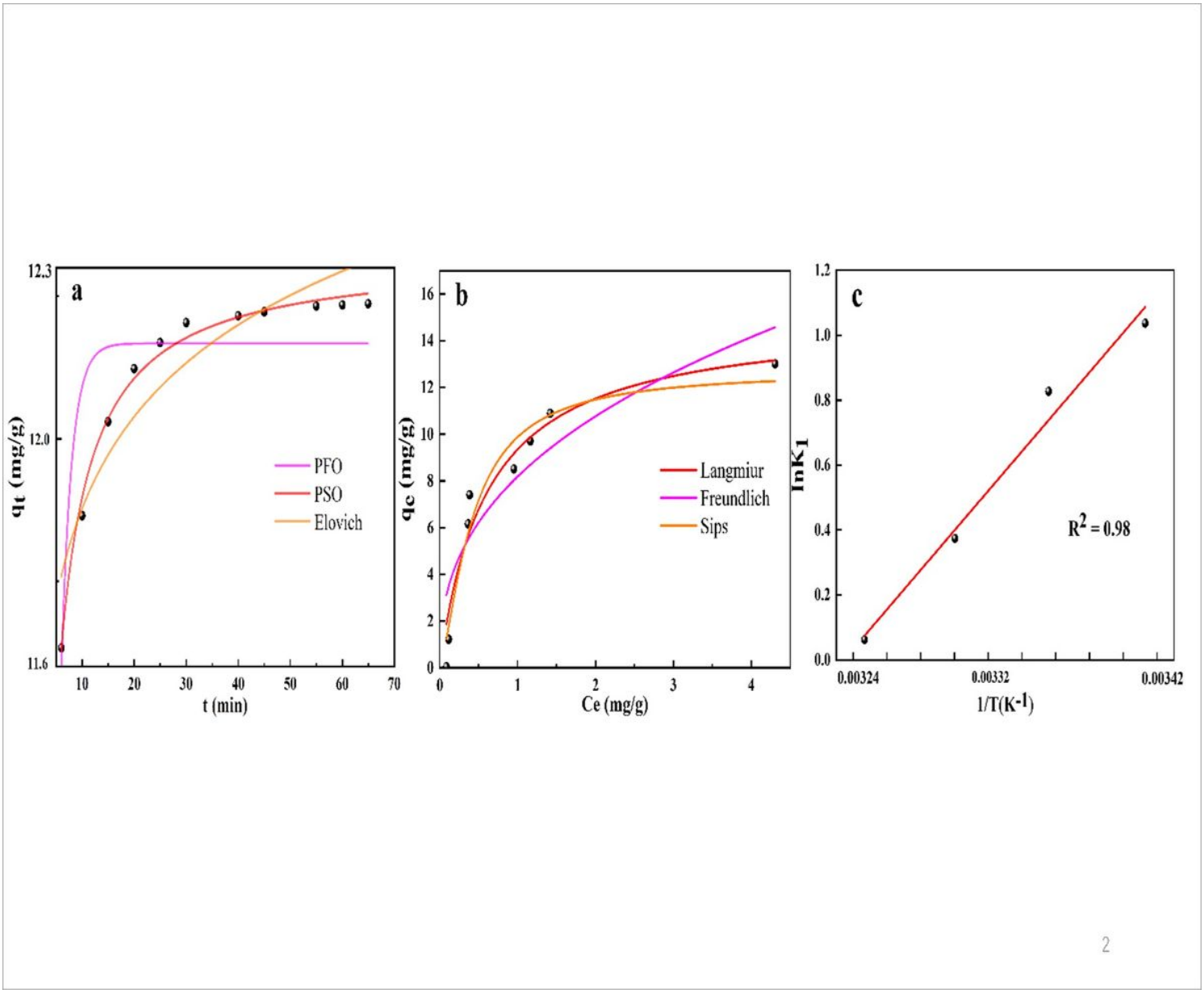

Figure 2

Adsorption kinetics (a), adsorption isotherms (b), and adsorption thermodynamics (c).

of Pb^{2+} on CROF.

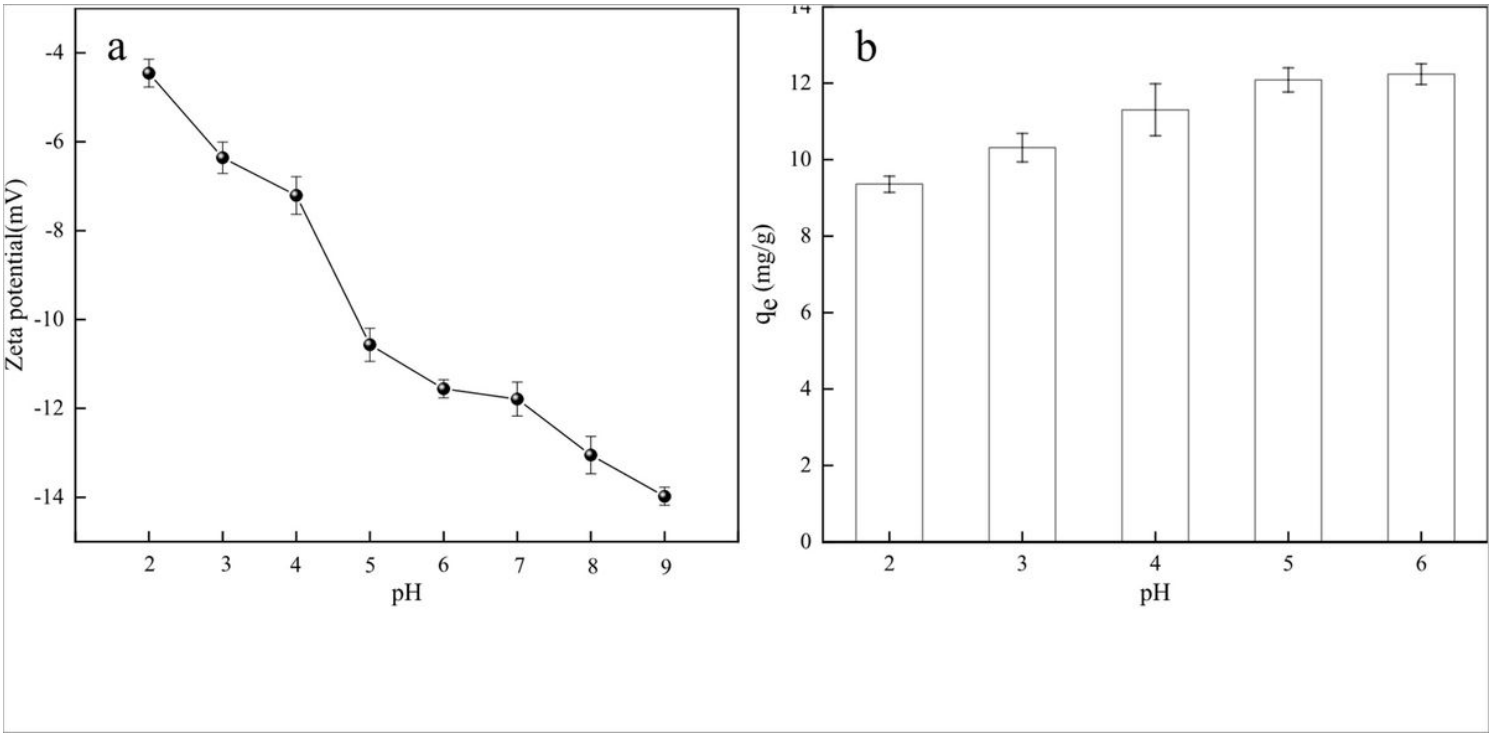

Figure 3

Zeta potentials of CROF (a) and effect of initial pH on adsorption capability (b).

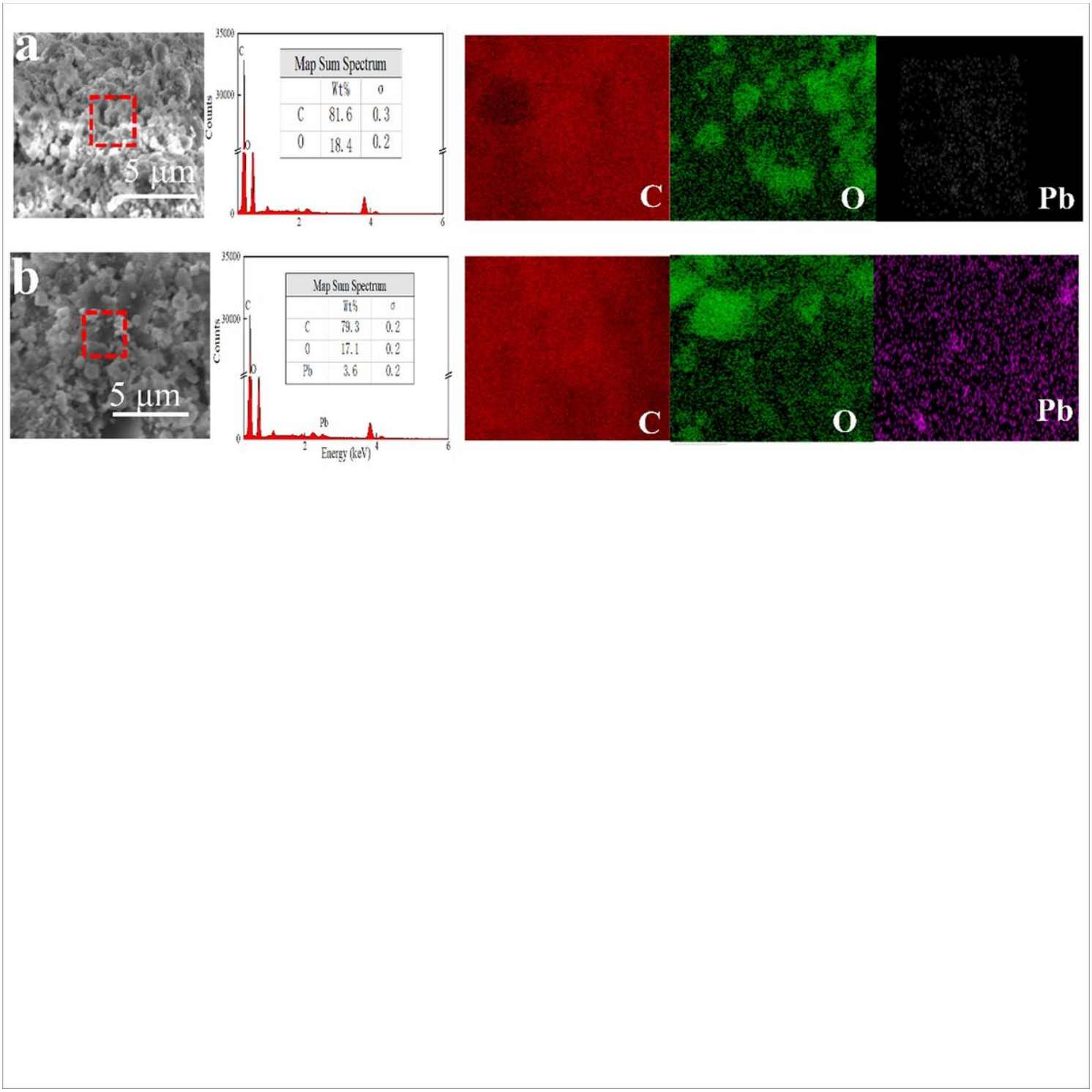

Figure 4

SEM-EDS spectrum of CROF before (a) and after (b) treated with 50.0 mg/L Pb^{2+}.

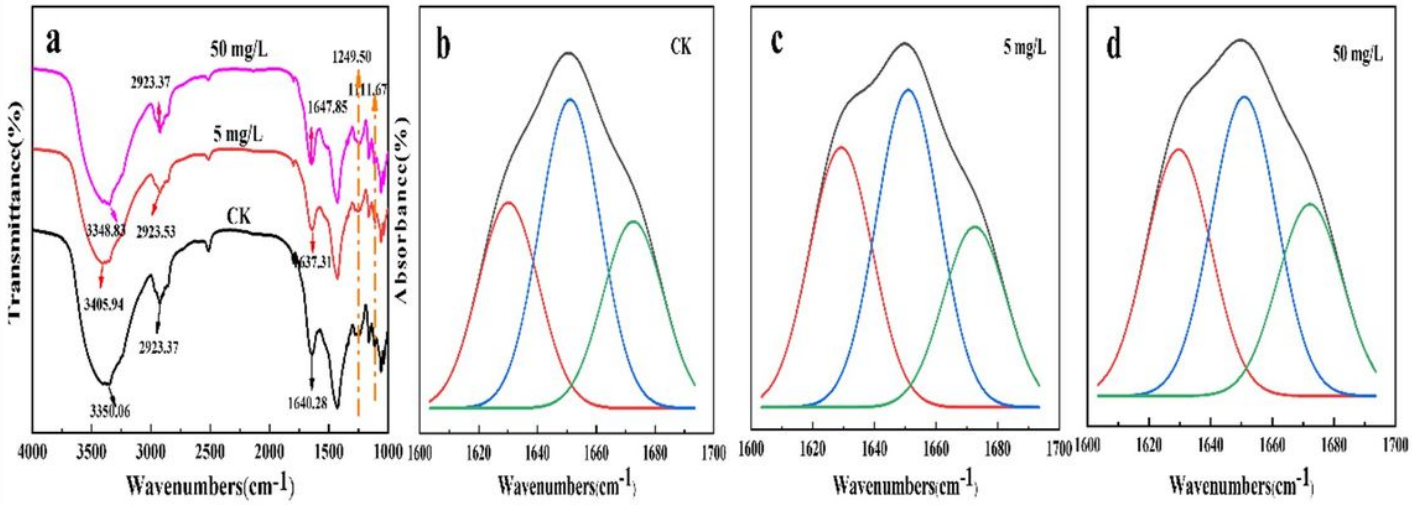

Figure 5

The FTIR pectra of CROF (a) and and second derivative resolution-enhanced curve-fitted amide I of CROF (b, c, d) treated with 0, 5.0, and 50 mg/L Pb^{2+}.

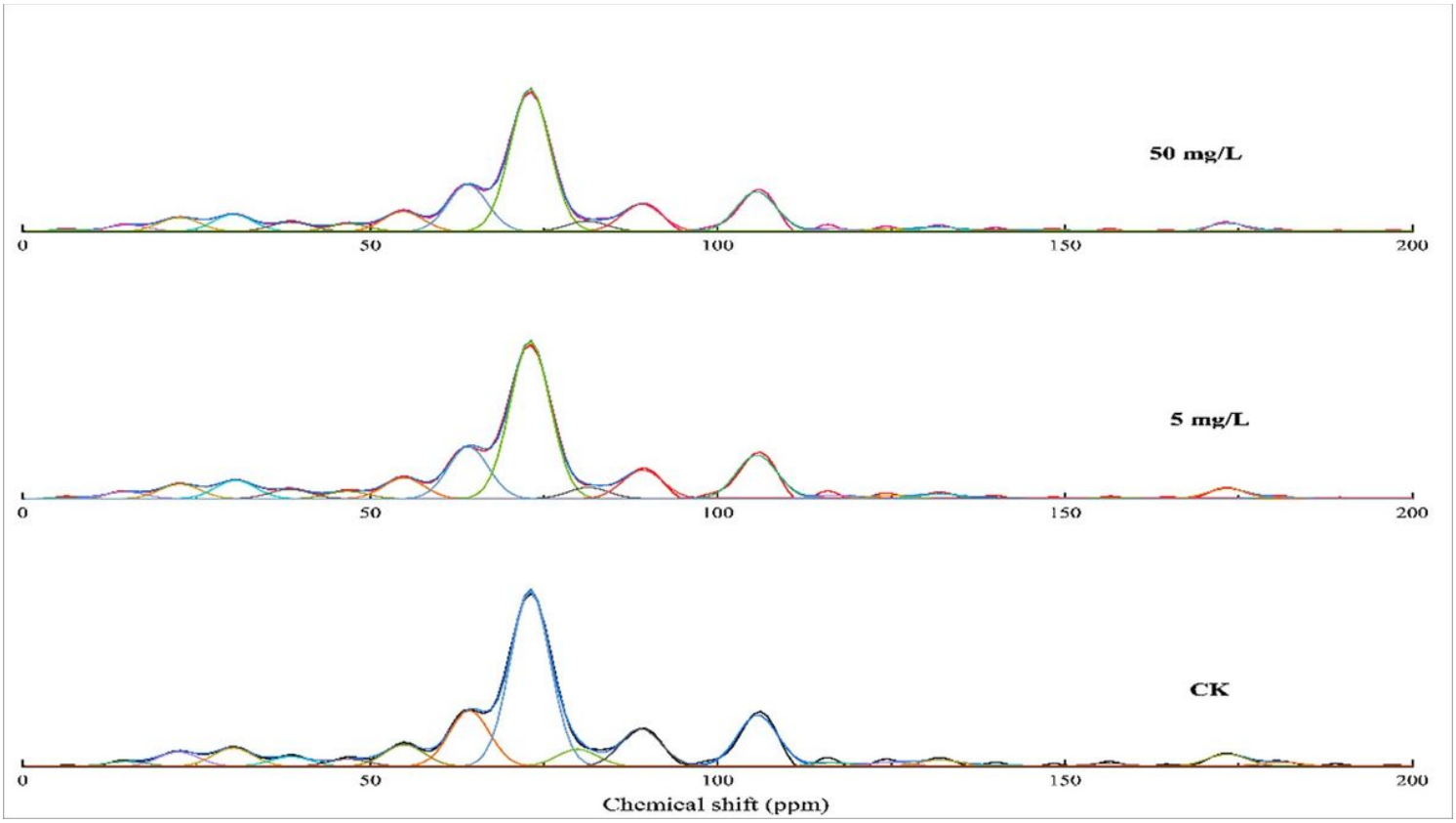

Figure 6

^{13}C NMR spectra of CROF treated with 0, 5.0, and 50 mg/L Pb^{2+}.

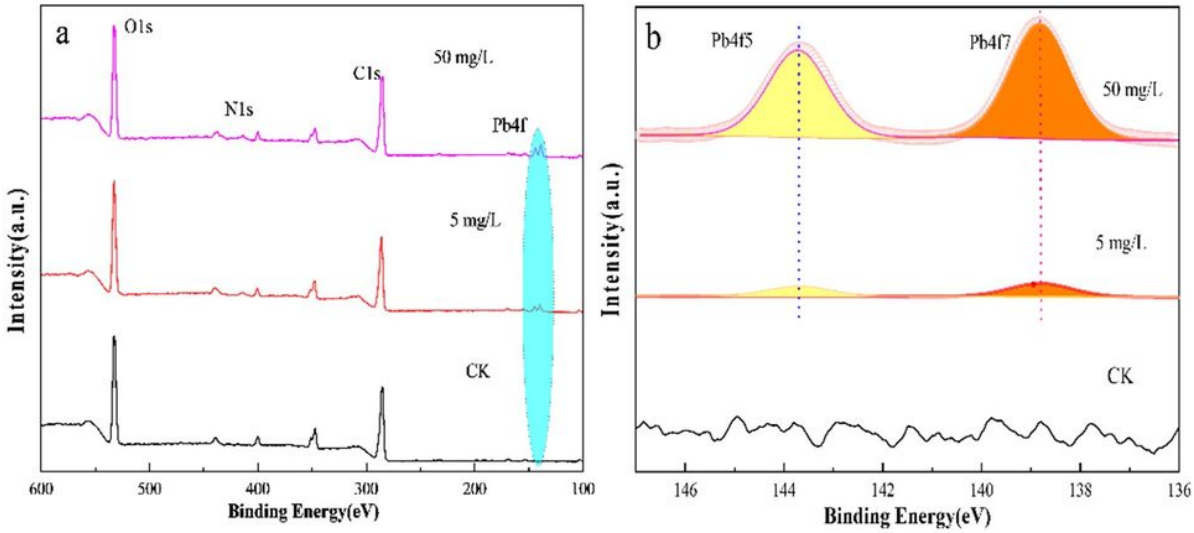

Figure 7

The XPS survey spectra (b), Pb4f spectra (b) of CROF treated with 0, 5.0, and 50 mg/L Pb^{2+}.

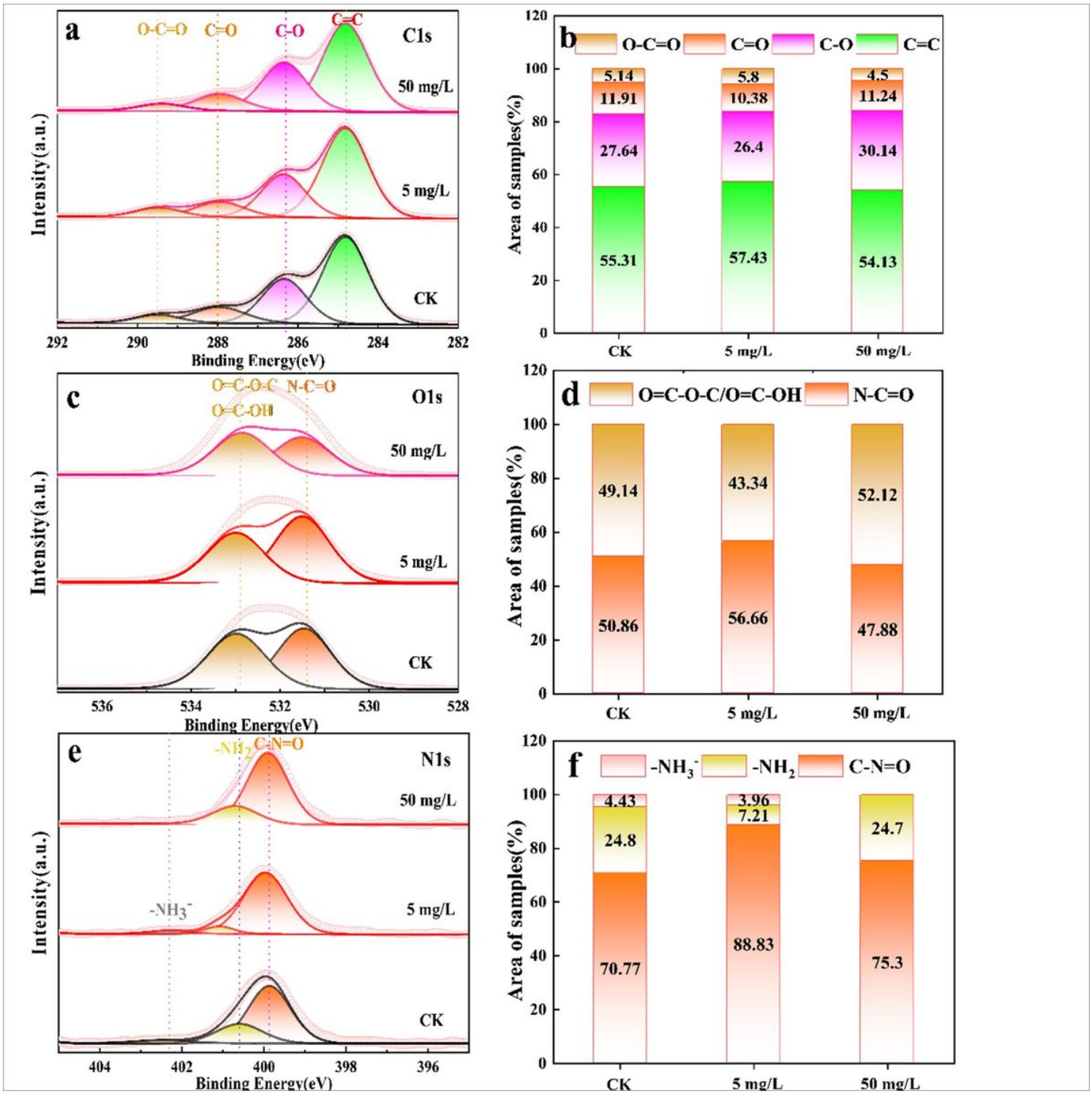

Figure 8

C1s spectra (a), O1s spectra (c), and N1s spectra (e) of CROF treated with 0, 5.0, and 50 mg/L Pb^{2+}, and corresponding of functional groups proportion of C1s spectra (b), O1s spectra (d), and N1s spectra (f).

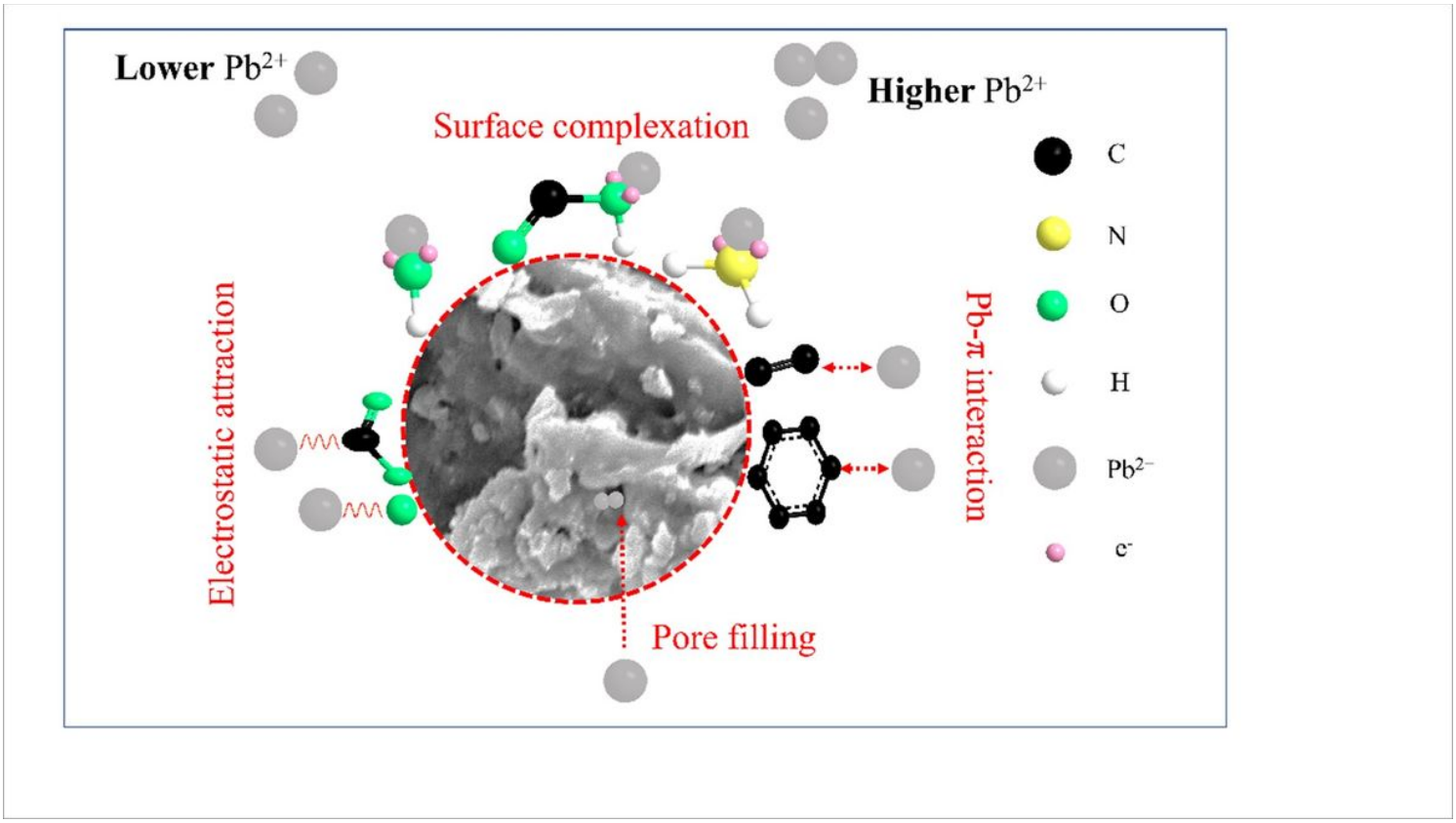

Figure 9

The simulation process of CROF adsorb Pb^{2+}.

Supplementary Files

This is a list of supplementary files associated with this preprint. Click to download.

- Table1.docx
- Table2.docx
- Table3.docx
- Table4.docx
- Table5.docx
- Fig.S1.docx